International Journal of Heat and Mass Transfer 204 (2023) 123865

Contents lists available at ScienceDirect

International Journal of Heat and Mass Transfer

journal homepage: www.elsevier.com/locate/hmt

Surface charge enhanced kinetically-limited evaporation in nanopores

Chu-Yao Chou, Chuanhua Duan*

Department of Mechanical Engineering, Boston University, United States

ARTICLE INFO

Article history:
Received 15 September 2022
Revised 10 December 2022
Accepted 11 January 2023
Available online 22 January 2023

Keywords:
Surface charge
Electrostatic disjoining pressure
Nanopore
Thin film evaporation
Extended meniscus
Evaporation area

ABSTRACT

Understanding the fundamentals of the kinetically-limited water evaporation in nanopores is of significant importance to improve the performance of modern evaporation-based thermal management devices. However, the ubiquitous existence of ions in aqueous solutions and charged function groups on solid walls have been ignored traditionally and the effect of surface charges on nanopore evaporation remains elusive. Herein, we consider the effect of surface charges on disjoining pressure and solve the system of equations governing the heat and mass transfer during the evaporation process from single nanopores numerically to yield the ultimate evaporation under various working conditions. Our results reveal that the surface charge, along with pore radius, wall temperature, and the relative humidity of ambient air, plays a critical role in determining the overall performance of the system. As the surface charge density increases, or as the pore radius decreases, the extended meniscus leads to a higher net rate of evaporation per unit pore area. Increasing the pore wall temperature increases the driving force for evaporation and results in a better performance despite the meniscus contracted. Results of this work provide new understanding of nanoscale phase-change heat transfer and is beneficial to applications requiring intensive evaporation, such as electronic cooling, forward osmosis, and membrane distillation.

1. Introduction

Evaporation, defined as the process of a material transforming from the liquid state to the vapor state, is a critical mechanism that governs the performance of evaporative cooling for electronic devices [1–3], steam generation for solar power plants [4–6], evaporation-based seawater desalination [7,8] and electrokinetic energy harvesting [9]. One way to enhance the performance of these systems is to exploit evaporation from nanoporous membranes because of its superior potential to dissipate heat and generate vapor efficiently. It has been reported that the evaporation heat fluxes, defined as the heat rate dissipated per unit area, can be as high as 600 [$\mathbf{W/cm^2}$] [10,11]. Furthermore, Li et al. experimentally demonstrated that the evaporation flux from nanopores depends critically on the pore diameter [12]. To explain this interesting observation, they discussed possible mechanisms including change of evaporation area due to surface-liquid interactions as well as change of evaporation coefficient σ_e (defined as the fraction of the vapor molecules crossing the liquid-vapor interface due to evaporation) due to the presence of surface charges on nanopore walls. However, no quantitative analysis was proposed to explain this phenomenon. The purpose of this study is to theoretically investigate the first mechanism, i.e., how surface charges affect the kinetically-limited evaporation through the extended meniscus and the resulting evaporation area. This analysis could fundamentally unravel the complex interaction between solid, liquid and dissolved ions confined in the nanopore, and the result drawn from this study could further guide designs for novel phase-change based devices.

It is well known that the length scale of the pore diameter plays the most important role in establishing the physical model to describe the heat and mass transfer process of evaporation from nanopores. Generally speaking, the capillary force attributed to the surface tension and the curvature of the meniscus dominates when the pore diameter is above 1 μm while the long-range van der Waals force prevails above 10 nm for non-polar liquids [13]. A large volume of the literature has modeled evaporation from microchannels and cylindrical tubes based on the two forces [14–21]. A novel study done by Narayanan et al. revealed that in addition to the above forces, electrostatic forces arose in polar liquids in fact increases the evaporation flux from nanopores dramatically [22]. The reason is that the electrostatic force acting on the interface tends to expand the area of the liquid meniscus. Therefore, as the area for evaporation increases, the evaporation mass flux normalized by the pore area increases. Inspired by this work, Pati et al. include the effect of slip velocity [23] while Lu et al. extend Narayanan's work to study the nonequilibrium and nonlocal effects of evaporation from nanopores [24]. Later, Lu et al. compares the

* Corresponding author.
E-mail address: duan@bu.edu (C. Duan).

https://doi.org/10.1016/j.ijheatmasstransfer.2023.123865
0017-9310/

Nomenclature

Parameters

$\dot{m}$	mass flow rate
$\dot{m}''$	mass flux
ϵ	absolute permittivity
$\hat{\sigma}$	accommodation coefficient
κ	local mean curvature
μ_i	chemical potential of ion i
μ_l	liquid viscosity
Π_d	disjoining pressure
ψ	electrical potential
ρ_l	liquid density
ρ_{xi}	number density of ions at a distance x away from the surface
σ	surface tension of water
σ_{lv}	surface charge density of the liquid-vapor interface
σ_{sl}	surface charge density of the solid-liquid interface
A	modified Hamaker constant
e	charge of one electron
k	Boltzmann constant
k_l	thermal conductivity of water
M	molar weight of water molecules
p_{atm}	ambient gas pressure
P_{ele}	disjoining pressure due to the electrostatic force
p_{li}	liquid pressure
P_{vdw}	disjoining pressure due to the van der Waals dispersion force
p_{vi}	equilibrium vapor pressure at the interface
p_v	partial pressure of vapor in the gas phase
q	heat flux
R	universal gas constant
r_c	pore radius
r_i	radial position of the liquid-vapor interface
s	entropy
T	absolute temperature of the ion solution
T_w	pore wall temperature
T_{li}	temperature of the liquid-vapor interface
T_v	ambient gas temperature
u_l	liquid velocity in the x-direction
u_{li}	liquid velocity in the x-direction at the liquid-vapor interface
v_i	specific number density
v_l	liquid velocity in the r-direction
v_{li}	liquid velocity in the r-direction at the liquid-vapor interface
w_{li}	liquid velocity in the direction normal to the liquid-vapor interface
z_i	charge number of ion i

experimentally measured kinetically-limited evaporation mass flux with the result of DSMC, the H-K equation and the Schrage equation [25]. The results show that given a constant accommodation factor, the Schrage equation coincides with the experimental results and the DSMC better than the the H-K equation. Therefore, the Schrage equation is used in the subsequent analysis to model the vapor transport to account for the nonequilibrium effect of intensive evaporation. However, these studies omitted the existence of a trace amount of protons and hydroxyl radicals in water as well as charged functional group on common surfaces. As a result, a modified electrostatic model to account for the complex solid-liquid-ion interaction is derived based on thermodynamic considerations in this study. This modified model is then incorporated with the systems of equations for fluid flow, heat transfer, and stress balance at the liquid-vapor interface in the continuum limit which are solved numerically to discover the effect of intermolecular forces between solid, liquid, and ions on the kinetically-limited evaporation.

2. Theoretical formulation

The system of interest is shown in Fig. 1(a), where the top and bottom boundaries of the figure are the walls of the nanopore. Liquid water comes into the control volume from the left boundary and water vapor exits from the right boundary. The vapor is exposed to a vacuum chamber at 150 Pa with a mixture of air-vapor at a temperature T_v. At steady-state, the evaporating meniscus inside a pore is generally divided into three regimes: (1) the absorbed thin film regime where the liquid is in equilibrium with the gas and no evaporation happens; (2) the thin-film regime where the disjoining pressure dominates over the capillary pressure; (3) the meniscus regime where capillary pressure is prevailing. Beyond the meniscus regime, the liquid is modeled as fully-developed, laminar flow, which is described by the Hagen-Poiseuille equation.

2.1. Conservation of mass at the evaporating interface

The mass transfer to the interface can be found as follow:

Assuming a steady, axisymmetric, incompressible flow, and neglecting the radial pressure gradient compared to the dominating capillary pressure, the axial component of the momentum balance for the liquid flow is given by

$$-\frac{dP_{li}}{dx}+\frac{\mu_l}{r}\frac{\partial}{\partial r}\left(r\frac{\partial u_l}{\partial r}\right)=0, \tag{1}$$

where p_{li} is the liquid pressure, μ_l is the liquid viscosity and u_l is the liquid velocity in the x-direction. The boundary conditions for fluid flow are the no-slip at the walls, $u=0$ at $r=r_c$, where r_c is the pore radius and the thermocapillary stress balance at the interface, $-\mu_l(\partial u)/(\partial r)=(\partial\sigma)/(\partial x)$ at $r=r_i$, where σ is the surface tension of water, r_i is the radial location of the meniscus. This boundary condition means that, the shear stress along the tangential direction of the liquid-vapor interface will be balanced by the tangential surface tension gradient due to possible temperature difference along the interface, which is the cause of thermal Marangoni flow and has been widely used in previous studies [21–23].

Using these boundary conditions, the solution of Eq. (1) is

$$u_l=\left(-\frac{1}{4\mu_l}\frac{dp_{li}}{dx}\right)\left(r_c^2-r^2+2r_i^2\ln\frac{r}{r_c}\right)-\frac{r_i}{\mu_l}\frac{\partial\sigma}{\partial x}\ln\frac{r}{r_c}, \tag{2}$$

To relate the evaporating mass flux at the interface with the water supply, we start with the mass conservation equation $\partial u_l/\partial x+(1/r)\partial(rv_l)/\partial r=0$ and integrate it between $r=r_i$ and $r=r_c$ to obtain the water supplied to the interface:

$$r_i v_{li}=\frac{d}{dx}\int_{r_i}^{r_c} ru_l dr+r_i u_{li}\frac{dr_i}{dx} \tag{3}$$

with the assumption that $v_l=0$ at $r=r_c$, where v_l is the liquid velocity in the r-direction and the subscript i denotes the interfacial property. Since the mass flow rate $\dot{m}=\int\rho_l u_l(2\pi r)dr=2\pi\rho_l\int u_l r dr$, where ρ_l is the density of the liquid, substituting $\int u_l r dr$ in Eq. (3) in terms of $\dot{m}$ gives

$$v_{li}=\frac{1}{2\pi\rho_l r_i}\frac{d\dot{m}}{dx}+u_{li}\frac{dr_i}{dx}. \tag{4}$$

From Fig. 1(b), the velocity normal to the interface w_{li} is given by

$$w_{li}=u_{li}\sin\theta-v_{li}\cos\theta, \tag{5}$$

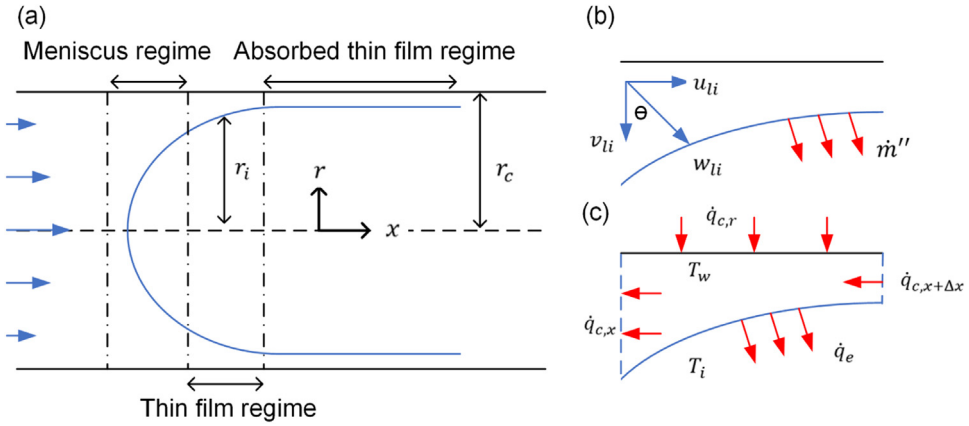

Fig. 1. (a) Cartoon of the water meniscus confined in a nanopore. (b) Velocity component of fluid velocity. (c) Control volume analysis of heat transfer.

where θ is the angle between the normal vector to the wall and the normal vector to the liquid-vapor interface as shown in Fig. 1(b). The supplying mass flux to the interface is therefore $\dot{m}'' = \rho_l w_{li} = \rho_l(u_{li}\sin\theta - v_{li}\cos\theta)$. Replacing v_{li} by Eq. (4), we get

$$\dot{m}'' = -\frac{1}{2\pi r_i}\frac{d\dot{m}}{dx}\cos\theta \tag{6}$$

as $dr_i/dx = \tan\theta$.

The mass flux leaving the interface at any point is described by the Schrage equation [26]:

$$\dot{m}'' = \frac{2\hat{\sigma}}{2-\hat{\sigma}}\left(\frac{M}{2\pi R}\right)^{1/2}\left(\frac{p_{vi}}{T_{li}^{1/2}} - \frac{p_v}{T_v^{1/2}}\right) \tag{7}$$

where $\hat{\sigma}$ is the accommodation coefficient and is assumed to be 0.3 in this work [25], $M = 0.018$ **[kg/mol]** is the molar weight of water molecules, $R = 8.314$ **[J/mol/K]** is the universal gas constant, p_{vi} is the equilibrium vapor pressure at the interface at a temperature of T_{li}, and p_v is the partial pressure of vapor in the gas phase at a temperature of T_v.

Equating $\dot{m}''$ with Eq. (7) and Eq. (6) and assuming the temperature discontinuity at the interface ($T_{li} = T_v$) is insignificant [21], we arrive at

$$-\frac{\cos\theta}{2\pi r_i}\frac{d\dot{m}}{dx} = \frac{2\hat{\sigma}}{2-\hat{\sigma}}\left(\frac{M}{2\pi R T_{li}}\right)^{1/2}(p_{vi} - p_v), \tag{8}$$

where $\cos\theta = 1/\sqrt{1+(dr_i/dx)^2}$. Substituting $\dot{m} = \int \rho_l u_l (2\pi r)dr$ and Eq. (2) in Eq. (8) and integrating the resulting equation between $r = r_i$ and $r = r_c$, we finally get an equation for $\dot{m}$ as

$$\begin{aligned}\dot{m} = {} & \frac{\pi\rho_l}{8\mu_l}\left(-\frac{-dp_{li}}{dx}\right)[(r_c^2 - r_i^2)(r_c^2 - 3r_i^2) - 4r_i^4\ln\frac{r_i}{r_c}] \\ & + \frac{\pi\rho_l}{8\mu_l}\left(\frac{d\sigma}{dT}\right)\left(\frac{dT_{li}}{dx}\right)[4r_i(r_c^2 - r_i^2) + 8r_i^3\ln\frac{r_i}{r_c}]\end{aligned} \tag{9}$$

Two unknowns (p_{li} and T_{li}) are present in Eq. (9) and more equations are needed to solve them.

2.2. Solve for the interface temperature T_{li}

Omitting the advective heat transfer [22,23], the energy conservation in the control volume shown in Fig. 1(c) is given by

$$q_{c,r} - q_{c,x} + q_{c,x+\delta x} = q_e, \tag{10}$$

where q_e is the rate of heat transfer from evaporation:

$$q_e = -h_{fg}\frac{d\dot{m}}{dx}\Delta x \tag{11}$$

Heat conduction from the pore wall reads

$$q_{c,r} = -k_l(2\pi r_c \Delta x)\left(\frac{\partial T_l}{\partial r}\right)_w \tag{12}$$

The total heat transfer in the x-direction reads

$$q_{c,x+\Delta x} - q_{c,x} \sim \Delta x\left(\frac{\partial q_{c,x}}{\partial x}\right), \tag{13}$$

where $\partial q_{c,x}/\partial x$ can be evaluated by the Leibniz integral rule as

$$\begin{aligned}\frac{\partial q_{c,x}}{\partial x} &= \frac{\partial}{\partial x}\int_{r_i}^{r_c} -k_l(2\pi r)\frac{\partial T_l}{\partial x}dr \\ &= (-2\pi k_l)\int_{r_i}^{r_c} r\frac{\partial^2 T_l}{\partial x^2}dr + (2\pi k_l r_i)\left(\frac{\partial T_l}{\partial x}\right)_i\frac{dr_i}{dx}\end{aligned} \tag{14}$$

A linear temperature profile is assumed for the temperature variation in the radial direction [21]:

$$\frac{T_l - T_w}{T_{li} - T_w} = \frac{r - r_c}{r_i - r_c}. \tag{15}$$

Substituting Eqs. (11), (12), (13), and (14) back to Eqs. (10) with (15), the governing equation for the temperature distribution is obtained:

$$\begin{aligned}&\frac{\pi k_l}{3}(r_c + 2r_i)(r_c - r_i)\left(\frac{\partial^2 T_{li}}{\partial x^2}\right) + \frac{2\pi k_l}{3}(r_c - r_i)\frac{\partial r_i}{\partial x}\frac{\partial T_{li}}{\partial x} \\ &+ \frac{2\pi k_l}{3}(T_{li} - T_w)\left(\frac{\partial r_i}{\partial x}\right)^2 - \\ &\frac{\pi k_l}{3}(r_c + 2r_i)(T_w - T_{li})\frac{\partial^2 r_i}{\partial x^2} + 2\pi k_l r_c\frac{t_w - T_{li}}{r_c - r_i} = -h_{fg}\frac{d\dot{m}}{dx}\end{aligned} \tag{16}$$

where the detailed derivation can be referred to [22].

2.3. Solve for the liquid pressure p_{li}

To find the liquid pressure p_{li}, we look at the pressure balance at the interface:

$$p_{atm} - p_{li} = 2\sigma\kappa + \Pi_d, \tag{17}$$

where p_{atm} is the ambient pressure, p_{li} is the liquid pressure at the interface, κ is the local mean curvature [27] and Π_d is the disjoining pressure [28,29].

$$\kappa = \frac{1}{2}\left(\frac{1}{r_i[1+(dr_i/dx)^2]^{1/2}} + \frac{d^2r_i/dx^2}{[1+(dr_i/dx)^2]^{3/2}}\right) \tag{18}$$

$$\Pi_d = P_{vdw} + P_{ele}, \tag{19}$$

where P_{vdw} is the pressure inside the liquid due to the van der Waals dispersion force between the liquid molecules and the solid

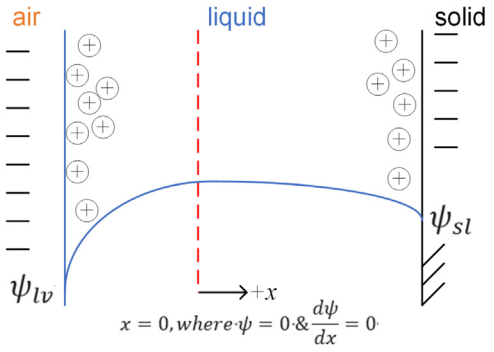

Fig. 2. The system of interest to derive P_{ele}. The blue solid line represents the electrical potential distribution between the two surfaces (not to scale). Note that both surfaces are negatively charged. (For interpretation of the references to colour in this figure legend, the reader is referred to the web version of this article.)

wall and P_{ele} is the pressure inside the liquid attributed to the electrostatic force acting between the dissolved ions and the solid wall. Assuming a Lennard-Jones interaction potential between the solid and the liquid molecules, we find $P_{vdw} = -A/6\pi\,(r_c - r_i)^3$, where $A = -3.148e^{-20}$[**J**] is the modified Hamaker constant [30].

It is note worthy of the sign convention used here - a positive value of P_{vdw} indicates the liquid molecules are attracted to the wall molecules. Therefore, a negative value of A means that the wall material is hydrophilic in nature.

Two distinct solutions may be derived for P_{ele} depending on the screening effect of the liquid film [31]. As the thickness of the film becomes thick enough, the thick water film screens the electrostatic force originating from the charged functional groups on the surface and P_{ele} would be independent of the surface charge density. On the other hand, P_{ele} would be dependent on the surface charge density as the water film is not thick enough to screen the electrostatic force. In the below paragraphs, we would discuss which solution is suitable for this study.

The system of interest is shown in Fig. 2, where the liquid solution is bounded by two surfaces - the solid-liquid interface and the liquid-vapor interface. To find P_{ele} we start with the chemical potential of different types of ions i in the solution [31], $\mu_i = z_i e\psi + kT\log\rho_{xi}$, where z_i is the charge number, e is the charge of one electron, ψ is the electrical potential, k is the Boltzmann constant, T is the absolute temperature, and ρ_{xi} is the number density of ions at an arbitrary location x. This equation is valid for all types of ions in the solution. The solid-liquid interface and the liquid-vapor interface have a surface charge density of σ_{sl} and σ_{lv}, respectively, and the corresponding electrical potentials are ψ_{sl} and ψ_{lv}, respectively. The liquid-vapor interface is considered to be negatively charged with $\sigma_{lv} = -2.4$ [$\mathbf{mC/m^2}$] [32]. On the other hand, a typical solid surface is also considered to be negatively charged with σ_{sl} ranging from 0 to -50 [$\mathbf{mC/m^2}$] for silica, carboxyl, and sulfate surfaces [33]. Since both surfaces are considered to be negatively charged, there would be a point between the two surfaces where the electrical potential is the maximum, *i.e.* $d\psi/dx = 0$. We set the plane where $d\psi/dx = 0$ to $x = 0$ and also set $\psi = 0$ at this plane. Assuming the system is in equilibrium and the surface charge densities σ_{sl} and σ_{lv} are constants, we have the Boltzmann distribution for

$$\rho_{xi} = \rho_{0i}\exp\left(-z_i e\psi/kT_l\right), \tag{20}$$

where ρ_{0i} is the number density of ion i at $x = 0$. The well-known Poisson equation for the net excess charge density at x reads

$$-\epsilon\nabla^2\psi = \Sigma_i z_i e\rho_{xi}, \tag{21}$$

where ϵ is the absolute permittivity of the solution, which when combined with the Boltzmann distribution, gives the Poisson-Boltzmann (PB) equation

$$\nabla^2\psi = -\frac{\Sigma_i z_i e\rho_{xi}}{\epsilon} \tag{22}$$

Differentiating Eq. (20) with x and sum over all the species of ions in the solution, we have

$$\frac{d\Sigma_i\rho_{xi}}{dx} = \frac{\epsilon}{2kT_l}\frac{d}{dx}\left(\frac{d\psi}{dx}\right)^2. \tag{23}$$

Integrating the above expression from $x = 0$ to $x = x$,

$$\Sigma_i\rho_{xi} - \Sigma_i\rho_{0i} = \frac{\epsilon}{2kT_l}\left(\frac{d\psi}{dx}\right)_x^2. \tag{24}$$

The Gibbs-Duhem equation states that $d\mu_i = -sdT_l + v_i dP$, where v_i is the specific number density [$\mathbf{m^3/(number\ of\ ions)}$], s is the entropy of the system. Under isothermal assumptions and at a fixed point x in the solution, $(d\mu_i/dP)_{x,T} = (1/\rho_{xi})_{x,T}$. Differentiating both sides with x', the distance between the solid-liquid interface and the liquid-vapor interface, we have $(dP/dx')_{x,T} = (\rho_{xi}d\mu_i/dx')_{x,T}$. We could use this equation to find the pressure of the counterions. The change in pressure at x on bringing two surfaces together from infinity ($x' = \infty$ and $P = 0$) to a distance of $x' = D$ is obtained as

$$\int_{x'=\infty}^{x'=D} dP = \Sigma_i\int_{x'=\infty}^{x'=D}\rho_{xi}\frac{d\mu_i}{dx'}dx' \tag{25}$$

$$P_x(D) = -\Sigma_i\int_{x'=D}^{x'=\infty}\left[z_i e\rho_i(d\psi/dx')_x dx' + kT_l d\rho_{xi}\right] \tag{26}$$

Using Eq. (22) with some manipulation, Eq. (26) becomes

$$P_x(D) = \left[-\frac{1}{2}\epsilon\left(\frac{d\psi}{dx}\right)^2_{x(D)} + kT_l\Sigma_i\rho_{xi}(D)\right] - \left[-\frac{1}{2}\epsilon\left(\frac{d\psi}{dx}\right)^2_{x(\infty)} + kT_l\Sigma_i\rho_{xi}(\infty)\right]. \tag{27}$$

Using Eq. (24) to substitute for $\Sigma_i\rho_{xi}(D)$, we find

$$P_{x(D)} = kT_l\Sigma_i\rho_{0i}(D) \tag{28}$$

since in the bulk solution when the two surfaces are separately infinitely far away, the ion concentration tends to zero, $\Sigma_i\rho_{xi}(\infty) = 0$. Therefore, the problem of finding the pressure between the two surfaces reduces to finding the total number density of the ions at a separation distance of D.

As the Debye length of pure water (pH=7) is on the order of 1 [μ**m**], the electrical double layer would cover the whole nanopore regime (pore radius ranging from 10 to 300 [**nm**]) and expel the co-ions out of the pore regime. Thus, applying charge conservation inside the thin film regime and neglecting the concentration of the co-ions,

$$ze\rho_{counterion}(D)(\pi r_c^2 - \pi r_i^2)l + \sigma_{sl}(2\pi r_c)l + \sigma_{lv}(2\pi r_i)l = 0. \tag{29}$$

we have

$$\rho_{counterion}(D) = \frac{-2(\sigma_{sl}r_c + \sigma_{lv}r_i)}{ze(r_c^2 - r_i^2)} = \Sigma_i\rho_{0i}(D). \tag{30}$$

Substituting Eq. (30) back to Eq. (28), we find

$$P_{ele} = \frac{-2kT_l(\sigma_{sl}r_c + \sigma_{lv}r_i)}{ze(r_c^2 - r_i^2)}. \tag{31}$$

Note that since $(\sigma_{sl}r_c + \sigma_{lv}r_i)/z$ is always negative, P_{ele} is always positive. The physical meaning of this is that by adding ions into the solution, the liquid becomes more attracted to the solid wall since the wall and counterions attract each other by the electrostatic force. This is also termed as the *Osmotic limit* as the liquid

film approaches zero thickness [31]. Therefore, the disjoining pressure could be expressed as

$$\Pi_d = \frac{-A}{6\pi\,(r_c - r_i)^3} + \frac{-2kT_l(\sigma_{sl}r_c + \sigma_{lv}r_i)}{ze(r_c^2 - r_i^2)}. \tag{32}$$

The other extreme case for thick wetting films leads to the conventional terms of $P_{ele} = (\epsilon/2(r_c - r_i)^2)(\pi kT_l/ze)^2$ used extensively in the literature and the derivation is as follows [22–24]:

Setting the coordinate system to $x = 0$ at the mid-plane and $x = \pm D/2$ at the two surfaces, we proceed by solving the PB equation (Eq. (22)) with two additional critical assumptions, i.e., only counterions are present in the solution ($i = 1$) and both the surfaces have identical surface potentials. The solution is given in [31]:

$$\psi = \frac{kT_l}{ze}\log\left(\cos^2(Kx)\right), \tag{33}$$

where K is a given by

$$K^2 = \frac{(ze)^2\rho_0}{2\epsilon kT_l}. \tag{34}$$

Since $i = 1$, Eq. (28) simply reduces to $P_{ele} = kT_l\rho_0 = 2\epsilon(kT_l/ze)^2K^2$. To find the limiting value of K, we differentiate Eq. (33) at $x = \pm D/2$ and we find:

$$\left(\frac{d\psi}{dx}\right)_{surface} = \frac{2kT_lK}{ze}\tan(KD/2). \tag{35}$$

As $D \to \infty$ for thick liquid films, K should approach π/D to keep $\tan(KD/2)$ finite in Eq. (35). Thus,

$$P_{ele,\ thick\ film} = \frac{\epsilon}{2(r_c - r_i)^2}\left(\frac{\pi kT_l}{ze}\right)^2. \tag{36}$$

This equation is known as the *Langmuir equation*. The major difference between the *Langmuir equation* and the *Osmotic limit* is that for the *Langmuir equation*, the P_{ele} is independent on the surface charge as the liquid film is thick enough to screen the effect of the electrostatic forces originating from the surface charges on the wall. Therefore, the *Langmuir equation* should only be applied to a thin film thickness (δ) where δ is much larger than the Debye length of the solution and only counterions are allowed to enter the liquid film. Hence the *Langmuir equation* is not suitable for this study and the *Osmotic limit* is a more appropriate expression.

2.4. Solving the system of equations

The governing Eqs. (8), (9), (16) and (17) form a set of complete equations that we can use to solve the meniscus profile, interface temperature T_i, liquid pressure p_{li}, as well as the total evaporation rate $\dot{m}$. It is clear from this set of equations that the heat and mass transfer are coupled in three different ways. First, from Eq. (9), the temperature gradient along the x-direction would change the mass flow rate by affecting the surface tension. Secondly, from Eq. (17), the local temperature would also affect the electrostatic disjoining pressure, which is part of the driving force for mass flow. Thirdly, from Eq. (16), the temperature profile of the pore wall is directly correlated to the evaporative heat dissipation.To solve these equations, Eqs. (8), (9), (16) and (17) are first nondimensionalized by $\bar{x} = x/r_c$, $\bar{r} = r_i/r_c$, $\bar{p} = p_{li}/p_v$, $\bar{\dot{m}} = \dot{m}/\dot{m}_0$, and $\bar{T}_{li} = 2\pi r_c k_l(T_{li} - T_w)/\dot{m}_0h_{fg}$, where $\dot{m}_0$ equals to

$$\dot{m}_0 = \frac{2\hat{\sigma}}{2 - \hat{\sigma}}\left(\frac{M}{2\pi RT_w}\right)^{1/2}[p_{vi}(T_w) - p_v](2\pi r_c^2). \tag{37}$$

The four governing equations in their nondimensional forms are (we drop the bar for simplicity):

$$\dot{m}\frac{dx}{dr} = \Pi_1\left(-\frac{dP}{dr}\right)[(1 - r^2)(1 - 3r^3) - 4r^{-4}\ln(r)] + \Pi_2\left(\frac{dT_{li}}{dr}\right)[4r(1 - r^2) + 8r^3\ln r] \tag{38}$$

$$(1 + \Pi_3\Pi_4T_{li})(1 + \Pi_4T_{li})^{-1/2} = -\frac{1}{r\sqrt{1 + (dx/dr)^2}}\frac{d\dot{m}}{dr} \tag{39}$$

$$\Pi_5 - P = \Pi_6\left(\frac{dx/dr}{r\sqrt{1 + (dr/dx)^2}} + \frac{d^2x/dr^2}{(1 + (dx/dr)^2)^{3/2}}\right) + \frac{\Pi_7}{(1 - r)^3} + \Pi_8\left(\frac{(1 + \Pi_9r)(1 + \Pi_4T_{li})}{1 - r^2}\right) \tag{40}$$

$$-\frac{d\dot{m}}{dr}\left(\frac{dx}{dr}\right)^2 = -\frac{T_{li}}{1-r}\left(\frac{dx}{dr}\right)^3 + \frac{1}{3}T_{li}\left(\frac{dx}{dr}\right) + \frac{1}{3}(1 - r)\frac{dx}{dr}\frac{dT_{li}}{dr} - \frac{1}{6}(1 + 2r)T_{li}\frac{\partial^2x}{\partial r^2} + \frac{1}{6}(1 + 2r)(1 - r)\left[\left(\frac{dx}{dr}\right)\left(\frac{d^2T_{li}}{dr^2}\right) - \frac{d^2x}{dr^2}\frac{dT_{li}}{dr}\right]. \tag{41}$$

The nondimensional groups are:

$$\Pi_1 = \frac{\pi\rho_lr_c^3p_v}{8\mu_l\dot{m}_0} \tag{42}$$

$$\Pi_2 = \frac{\rho_lr_ch_{fg}}{16\mu_lk_l}\left(\frac{d\sigma}{dT_{li}}\right) \tag{43}$$

$$\Pi_3 = \frac{\rho_vh_{fg}}{p_{v,eq} - p_v} \tag{44}$$

$$\Pi_4 = \frac{\dot{m}_0h_{fg}r_c}{k_lT_w} \tag{45}$$

$$\Pi_5 = \frac{p_{atm}}{p_v} \tag{46}$$

$$\Pi_6 = \frac{\sigma}{r_cp_v} \tag{47}$$

$$\Pi_7 = \frac{-A}{6\pi r_c^3p_v} \tag{48}$$

$$\Pi_8 = \frac{-2kT_w\sigma_{sl}}{zer_cp_v} \tag{49}$$

$$\Pi_9 = \frac{\sigma_{lv}}{\sigma_{sl}} \tag{50}$$

The systems of ODEs are solved by ode45 in MATLAB and the boundary conditions at $x = 0$ for the problem is

1. $r = r_0 = r_c - t_0$, where t_0 is the absorbed thin film thickness.
2. $dr/dx = 0$ as the slop is assumed to be flat.
3. $\dot{m} = 0$ since no evaporation happens in the absorbed thin film regime.
4. $p = \Pi_5 - \Pi_6/r_0 - \Pi_7/(1 - r_0)^3 - \Pi_8(1 + \Pi_9r_0)/(1 - r_0^2)$.
5. $T = 0$, assuming $T_{li} = T_w$
6. $dT/dx = 0$

The absorbed thin film thickness t_0 is obtained by the same method as in [22] and is omitted here for brevity.

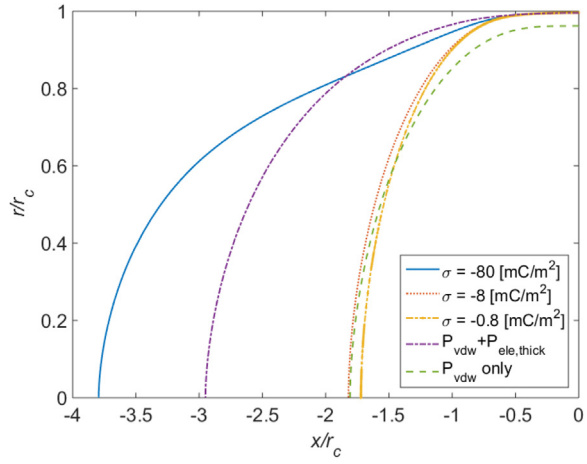

Fig. 3. Effect of the surface charge density on the shape of the water meniscus for $r_c = 50$ [**nm**], $T_w = 90$ °C, and $RH = 0.3$.

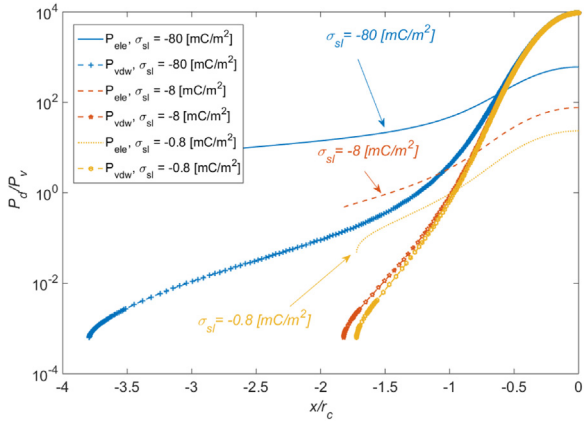

Fig. 4. Axial variation of the normalized disjoining pressure for different surface charges from -80 to -8, and -0.8 [**mC/m²**] with $r_c = 50$ [**nm**], $T_w = 90$ °C, and $RH = 0.3$. Same color represents the same surface charge. Lines with markers represent P_{vdw} while lines without markers represent P_{ele}.

3. Results and discussions

3.1. Effect of the solid-liquid surface charge density

The effect of the surface charge on the meniscus shape of the kinetically-limited evaporation is shown in Fig. 3, corresponding to $r_c = 50$ [**nm**], $T_w = 90$ °C, and $RH = 0.3$.

A typical surface charge density value is in the range from 0 to -50 [**mC/m²**] for silica, carboxyl, and sulfate surfaces [33]. Thus, the surface charge density value for σ_{sl} in this work is selected as -80, -8, and -0.8 [**mC/m²**] to demonstrate the effect of charges on the evaporation kinetics. Meanwhile, the surface charge density for the liquid-vapor interface is kept at a constant of -2.4 [**mC/m²**] unless stated otherwise. It is shown that as the magnitude of the charge density increases, the total interface area of the meniscus inside the nanopore increases. This is because the unique shape of the evaporating interface is the result of balancing the forces acting on the meniscus with the viscous pressure loss to supply enough water for evaporation. In addition, the meniscus shape with the Langmuir equation and with only the P_{vdw} term are also shown in the figure as the dash-dot purple line and the dash green line, respectively. An interesting observation is that the meniscus would be extended further than the Langmuir equation only with a surface charge density of -80 [**mC/m²**] while it barely extends with a surface charge density of -8 and -0.8 [**mC/m²**]. Near the center of the meniscus where the disjoining pressure decreases rapidly in magnitude as shown in Fig. 4, the meniscus must be highly curved to increase the capillary pressure gradient to sustain the required mass flux.

On the other hand, as the meniscus approaches the pore wall ($x/r_c \to 0$), the liquid film becomes thinner and the disjoining pressure significantly increases in magnitude. Therefore, the disjoining pressure gradient is large enough to drag sufficient water for evaporation and the meniscus becomes less curved. As a result, as long as we actively tune the disjoining pressure to a larger value, the meniscus would be further extended. In fact, we had demonstrated this via introducing a larger surface charge density on the wall as the wall attracts the ions with a stronger electrostatic force and increases the disjoining pressure. This could be justified by studying the magnitudes of the components of the disjoining pressure inside the liquid as shown in Fig. 4. As the surface is slightly charged ($\sigma_{sl} = -0.8$ [**mC/m²**]), P_{vdw} dominates P_{ele} as x/r_c is less than -1. However, as the charge density increases to -80 [**mC/m²**], the regime where P_{ele} prevails over P_{vdw} prolonged to $x/r_c \sim -0.5$ and drastically extends the meniscus area from $x/r_c \sim -1.8$ to $x/r_c \sim -3.8$ [34].

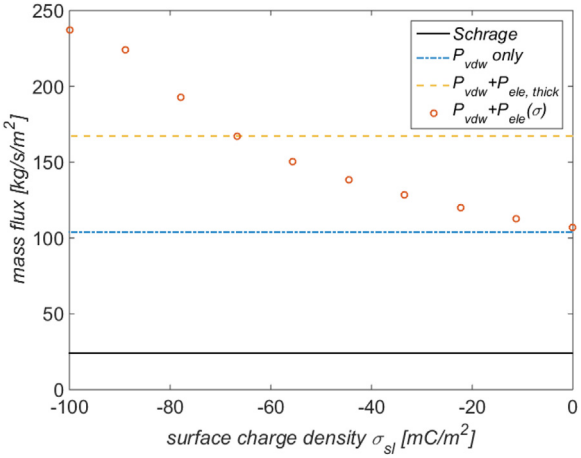

Fig. 5. The effect of surface charge on the evaporation mass flux from a nanopore (orange dots) for $r_c = 50$ [**nm**], $T_w = 90$ °C, and $RH = 0.3$. The mass flux increases monotonically as the magnitude of the surface charge increases. The blue line represents the mass flux from a nanopore without considering P_{ele}. (For interpretation of the references to colour in this figure legend, the reader is referred to the web version of this article.)

The corresponding mass flux evaporated from a charged nanopore is shown in Fig. 5. First, by considering the slightest extension of the meniscus due to P_{vdw} only, the mass flux has been increased from 24.12 to 103.85. This shows that the mass flux would be significantly underestimated with the Schrage equation alone, which represents the traditional limit of evaporation from nanopores. Secondly, it is observed that the mass flux increases from 107 to 237.4 [**kg/m²s**] monotonically as the magnitude of the surface charge increases from 0 to -100 [**mC/m²**]. This result is outstanding since we achieved a 121% increase in mass flux by simply charging the wall. The corresponding heat flux is 53.7 [**kW/cm²**], which greatly exceeds the required heat flux of 1 [**kW/cm²**] to dissipate heat from GaN-based electronics [35].

3.2. Effect of the liquid-vapor surface charge density

So far, we have only considered a constant surface charge density of -2.4 [**mC/m²**] on the liquid-vapor interface. However, this value is actually scattering from -2.4 to -70 [**mC/m²**] on the literature [32,36]. Therefore, we select $\sigma_{lv} = -2.4$, -36, and

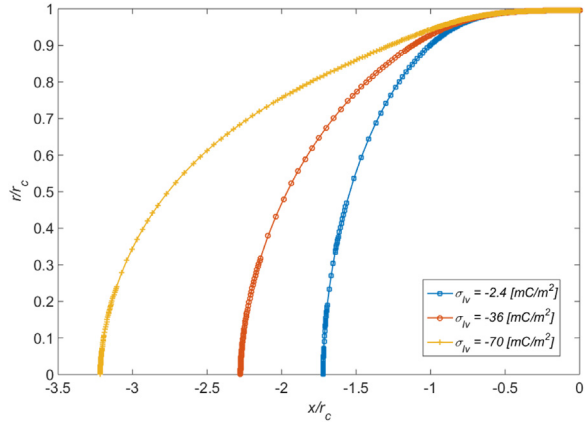

Fig. 6. The effect of the liquid-vapor surface charge density on the meniscus shape corresponding to $r = 50$ **nm**, $\sigma_{sl} = -0.8$ [**mC**/**m²**], $\hat{\sigma} = 0.3$, and $RH = 0.3$. The inset compares the average mass flux [**kg**/**m²s**] at different σ_{lv}.

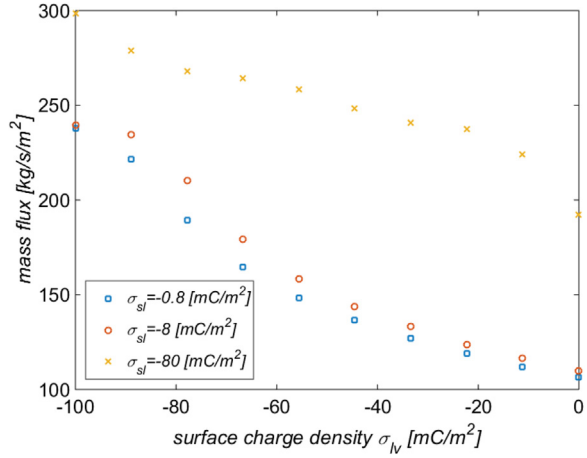

Fig. 7. The effect of surface charge density on the liquid-vapor interface σ_{sl} on the evaporation mass flux from a nanopore for $r_c = 50$ [**nm**], $T_w = 90$ °C, and $RH = 0.3$. The mass flux increases monotonically as the magnitude of σ_{sl} increases.

-70 [**mC**/**m²**] to demonstrate the effect of the liquid-vapor surface charge density on the meniscus shape. The results are plotted in Fig. 6 with $r = 50$ **nm**, $\sigma_{sl} = -0.8$ [**mC**/**m²**], $\hat{\sigma} = 0.3$ and $RH = 0.3$.

It is shown that increasing the surface charge density on the liquid surface has the exact same effect of increasing the surface charge density on the solid surface - the meniscus becomes further extended and the mass flux increases. We further plot the effect of the surface charge density on the liquid-vapor interface versus the mass flux in Fig. 7 at various σ_{sl}.

It can be shown that for all σ_{sl}, the mass flux increases as σ_{lv} increases. In addition, the maximum mass flux could reach up to 300 [**kg**/**m²s**] if the surface charge density of the liquid-vapor interface is -100 [**mC**/**m²**]. However, it remains illusive of what the exact value of the surface charge density on the liquid-vapor interface is in a nanopore. Further experimental study on this topic is encouraged in order to provide better quantitative predictions for realistic conditions.

3.3. Pore radius effect

Fig. 8 shows the effect of the pore radius on the meniscus shape for $T = 90$ °C and $RH = 0.3$. It is observed the meniscus becomes more extended as the pore radius reduces, and this trend is the same for different values of surface charge densities. As a result of the meniscus extension, smaller nanopores exhibit larger evaporation fluxes (see Fig. 8(b)). Taking $\sigma_{sl} = -8$ [**mC**/**m²**] as an example, the evaporation flux is only 86 [**kg**/**s**/**m²**] for the nanopore with a radius of 70 [**nm**], but reaches 293 [**kg**/**s**/**m²**] for the nanopore with a radius of 10 [**nm**]. One possible explanation for the more extended meniscus and larger evaporation flux in the smaller nanopore is that the disjoining pressure increases with the decreasing pore radius. To verify this explanation, we plot P_d (measured from the non-evaporating thin film) V.S. the pore radius in Fig. 9 with $T = 90$ °C, $RH = 0.3$ and $\hat{\sigma} = 0.3$. The orange diamond represents the data with $\sigma_{sl} = -8$ [**mC**/**m²**] while the blue triangle represents $\sigma_{sl} = -0.8$ [**mC**/**m²**]. Surprisingly, we actually found that P_d would slightly decrease with the decreasing radius, varying from 202 to 196 [**MPa**] as the pore radius decreases from 70 to 10 [**nm**]. This decreasing trend and the magnitude of the disjoining pressure is consistent with the previous modeling study reported by Narayanan et al. [22] The large disjoining pressure results from the ultrathin non-evaporating thin film thickness and the decreasing trend of the disjoining pressure can be attributed to the increasing non-evaporation thin film thickness in smaller nanopores [22]. As show in the inset figure of Fig. 9, the thickness of the non-evaporating thin film indeed slightly decreases as the pore radius increases. However, this trend is different from what has been reported in a recent experimental study by Zou et al. [37], where the water disjoining pressure in nanochannels was calculated based on wicking experiments and molecular dynamics (MD) simulation of contact angle. Also, the magnitude of our calculated disjoining pressure in nanopores is two orders of magnitude higher than their results in nanochannels. We attribute these difference to the difference in experiments (i.e., evaporation V.S. wicking), simulation methods (i.e., continuum modeling V.S. MD simulation), operating conditions (including temperature and humidity) as well as nanoconfinements (1-D confined nanochannel V.S. 2-D confined nanopores).

Nevertheless, our modeling results show that the increasing extension of the evaporation area in smaller nanopores does not stem from the increasing disjoining pressure. Instead, we believe that it is a result of relatively larger range of disjoining pressure in smaller nanopores. Fig. 10 shows the axial variation of capillary and disjoining pressure for nanopores of pore radii 10 and 70 [**nm**] at two different surface charge densities. It is clear that the disjoining pressure is significant over a larger portion of the interface in the smaller nanopore. At the surface charge density of -0.8 [**mC**/**m²**], the regimes where the magnitude of the disjoining pressure is significant ($P_d/P_v \geq 1$) ends at $x/r_c \sim -4.5$ for nanopore with a pore radius of 10 [**nm**] and at $x/r_c \sim -0.5$ for nanopore with a pore radius of 70 [**nm**], respectively. Consequently, fluid flow can be sustained over a relatively longer regions in smaller nanopores, leading to the more extended meniscus and the higher evaporation flux per pore area. It is worth noting that when the surface charge density increases to -8 [**mC**/**m²**], P_{ele} increases and the region where the disjoining pressure is significant becomes even larger, ending at $x/r_c \sim -5$. This further extension of the meniscus also leads to an increase in the evaporation mass flux as demonstrated in the inset of Fig. 8.

3.4. Thermocapillary stresses in nanopores with various surface charge densities

The effect of the thermocapillary stresses on the meniscus shape is presented in Fig. 11 at 90 °C with $RH = 0.3$.

The predictions with the thermocapillary stresses are plotted in solid lines while the results without the thermocapillary stresses are plotted in dotted markers. As shown in the figure, the thermocapillary effect has negligible effect on the meniscus shape for all of the cases considered (either 50 or 70 [**nm**] pores with -8 or -0.8 [**mC**/**m²**]). This can be justified by observing the temper-

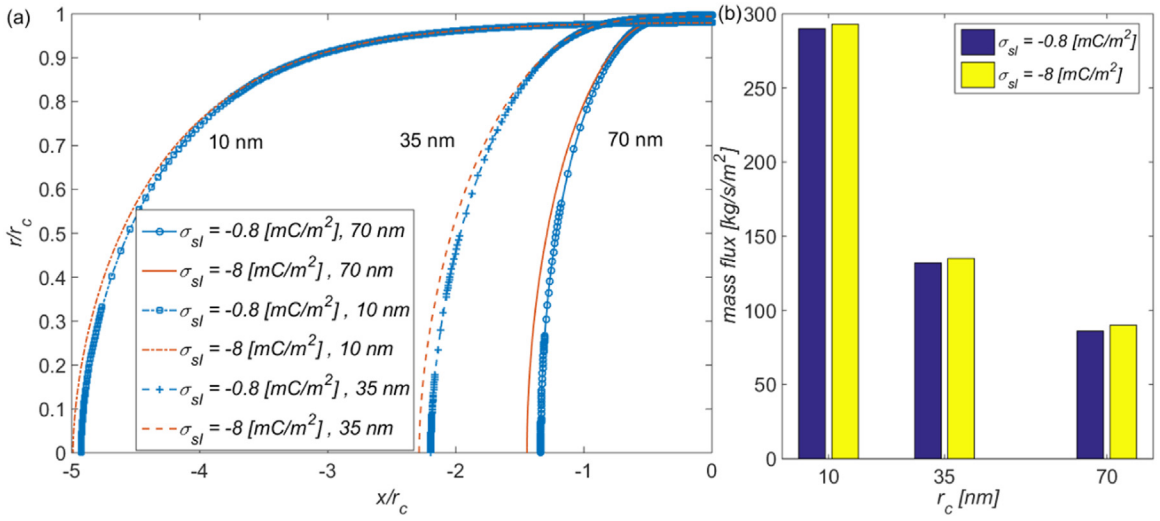

Fig. 8. Effect of pore radius on the meniscus shape and evaporation mass flux. (a) The radius effect on the meniscus shape with different surface charge densities corresponding to $T_w = 90$ °C and $RH = 0.3$. The dashed-dot lines represent $r = 10$ [**nm**]; the dashed lines represent $r = 35$ [**nm**]; the solid lines represent $r = 70$ [**nm**]. The lines with markers represent a surface charge density of -0.8 [**mC**/**m**^{2}] while lines without markers represent a surface charge density of -8 [**mC**/**m**^{2}]. (b) The corresponding evaporation mass flux at $T_w = 90$ °C and $RH = 0.3$.

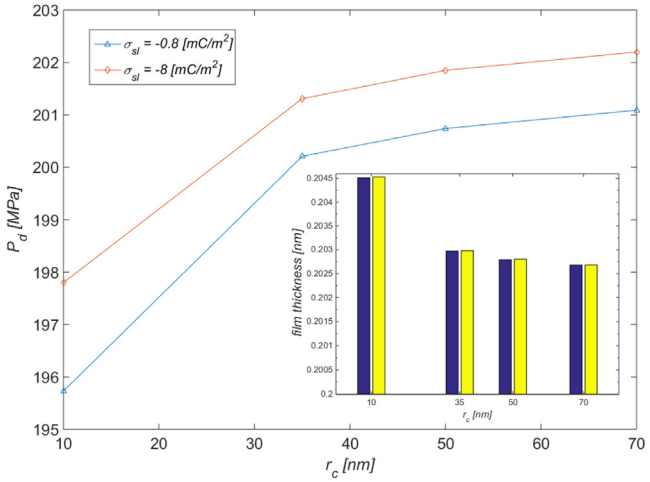

Fig. 9. The disjoining pressure versus the pore radius with different solid-liquid surface charge densities with $T = 90$°C, $RH = 0.3$, and $\hat{\sigma} = 0.3$. The inset figure shows the liquid film thickness versus the pore radius.

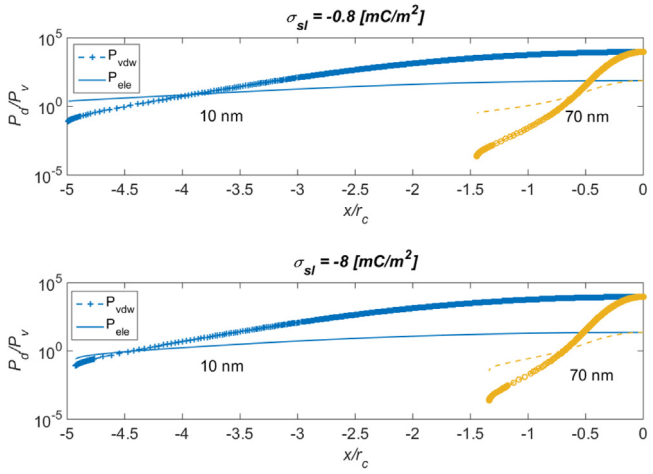

Fig. 10. Axial variation of the normalized disjoining pressure for different surface charges at -0.8 and -8 [**mC**/**m**^{2}] with different pore radius of 10 and 70 [**nm**] at $T_w = 90$ °C, and $RH = 0.3$. Same color represents the same radius. Lines with markers represent P_{vdw} while lines without markers represent P_{ele}.

Table 1
Temperature difference along the liquid-vapor interface.

max ΔT_{li}	50 [**nm**]	70 [**nm**]
-8 [**mC**/**m**^{2}]	2.0802 °C	3.2866 °C
-0.8 [**mC**/**m**^{2}]	2.5829 °C	3.9809 °C

ature change along the interface. The results are summarized in Table 1 and the maximum temperature change along the meniscus is 3.98 °C. The corresponding maximum surface tension change is 6.88×10^{-4} [**N**/**m**], which is around 1% of the original value and is negligible. These results show that the temperature gradient along the meniscus is not significant to affect the evaporation mass flux.

3.5. Temperature and relative humidity effect

Although the thermal capillary effect only causes negligible change of the evaporation area and evaporation flux, the operating temperature can still significantly affect the evaporation per-

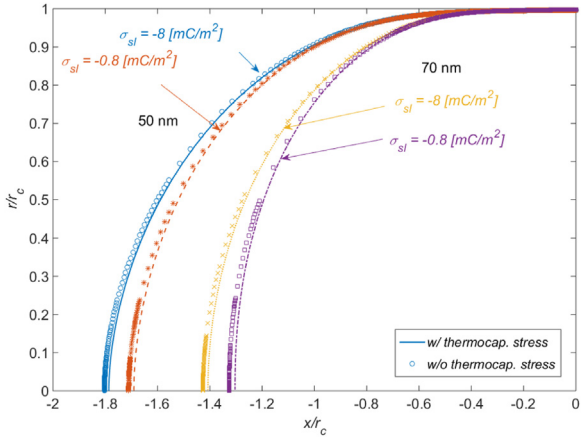

Fig. 11. The effect of the thermocapillary stresses on the meniscus shape with different surface charge densities corresponding to $T_w = 90$ °C and $RH = 0.3$. The lines represent results with thermocapillary stresses while the markers represent results without thermocapillary stresses.

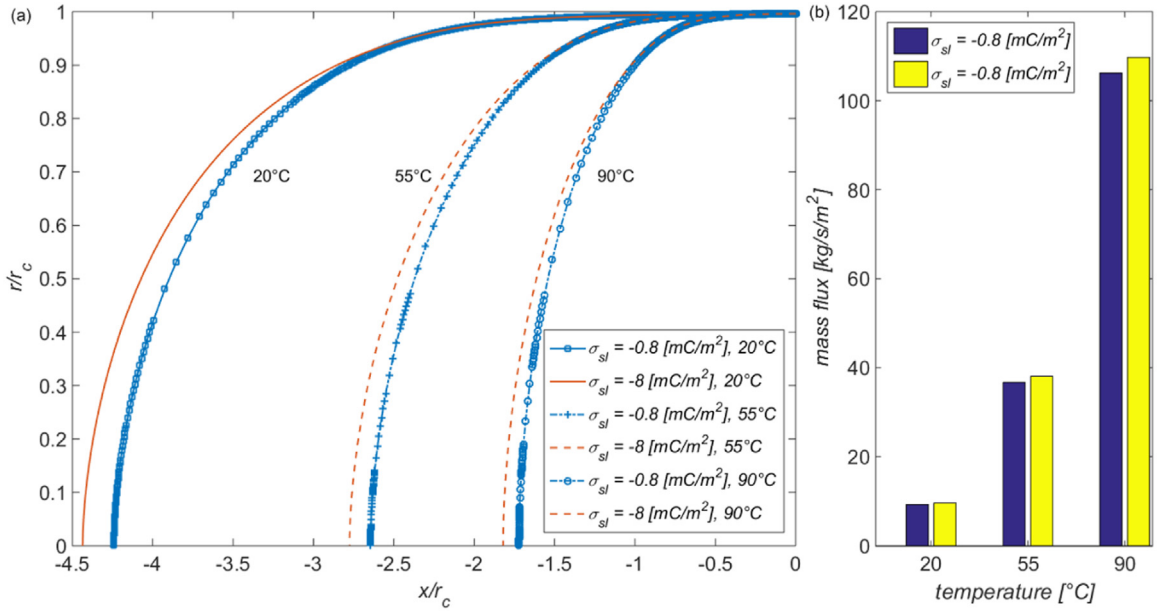

Fig. 12. Effect of temperature on the meniscus shape and evaporation flux. (a) The temperature effect on the meniscus shape with different surface charge densities corresponding to $r = 50$ [**nm**] and $RH = 0.3$. Lines with markers represent a surface charge density of -0.8 [$\mathbf{mC/m^2}$] while lines without markers represent a surface charge density of -8 [$\mathbf{mC/m^2}$]. (b) The corresponding evaporation mass flux [$\mathbf{kg/m^2s}$] at two different surface charge densities.

formance via the other two coupling mechanisms. Fig. 12 demonstrates the effect of the wall temperature on the meniscus shape and the evaporation mass flux with different surface charge densities with $r = 50$ **nm** and $RH = 0.3$.

It is observed that the length of the meniscus reduces as the temperature increases from 20 to 90 [°**C**] yet the average mass flux increases as the temperature increases. This dramatic jump in the performance is due to a higher vapor pressure at the interface. The magnitude of Π_8 decreases from 1.4286 to 0.0583. The decrease in this term results in a lower driving force for liquid flow into the thin film regime. Thus, the gradient of the curvature must be higher at a higher temperature to sustain a higher evaporation rate. This in turn results in a contraction of the meniscus. Interestingly, this trend is counter-intuitive and is in conflict with the results published in [24], where the meniscus shape should start flat and becomes fully extended as the temperature increases to drive more water to the meniscus area. Further experimental work is encouraged to justify this trend. In addition, the meniscus shape becomes more extended as the surface charge density increases at a given temperature. This is because that as the surface charge density increases, the disjoining pressure term increases, leading to a smaller gradient of curvature locally and extends the meniscus further. This results in an increase in the average mass flux as shown in Fig. 12b.

Fig. 13 shows the shape of the meniscus at different relative humidity and different surface charge densities. Notice that while the Schrage equation states that the mass flux from nanopores is linearly proportional to the relative humidity, the results from this study suggests a non-linear trend as shown in Fig. 13b.

The discrepancy comes from the consideration of the extended meniscus. In addition, the effect of increasing the relative humidity is to decrease the potential for evaporation and is analogous to the effect of decreasing the temperature. As a result, the meniscus extended further as the relative humidity increases.

3.6. Comparison with literature data

Fig. 14 compares the ratio between the theoretical mass flux obtained in this work at $T_w = 20$ [°**C**], $P_v = 150$ [**Pa**] and $RH = 0.3$ with the experimental data obtained in [12] as a function of the pore radius. The surface charge density reported in [12] is in the range from -2 to 0 [$\mathbf{mC/m^2}$] and the corresponding theoretical mass flux is relatively insensitive to the surface charge density in this range. Meanwhile, the surface charge density on the meniscus is assumed to be a constant at -2.4 [$\mathbf{mC/m^2}$] [32]. It is shown that the mass flux ratio ($\dot{m}''_{theo}/\dot{m}''_{\exp}$), which is an indicator of the degree of discrepancy between the theoretical value and the data, is larger than one, implying that all of the experiment data is below the theoretical value. More importantly, the mass flux ratio increases from 9.3 to 21.3 as the pore radius decreases from 152.3 to 13.9 [**nm**]. We believe the increase of the difference between the theoretical value and the data originates from the shape of the meniscus. Since the nanopore devices for the experimental studies are specifically designed to ensure that liquid transport to the evaporation interface is not the transport limit, the meniscus shape may not correspond to the fully extended case. In fact, based on the measured evaporation rates and the device dimensions, we can calculate the corresponding apparent contact angle for all the experimental cases. As shown in the inset of Fig. 14, the apparent contact angle actually increases from 21.2 to 83.8 as the nanopore radius decreases from 152.3 to 13.9 [**nm**], indicating that the meniscus is the flattest when the pore radius is 13.9 [nm]. In contrary, the theoretical model in this work calculates the fully extended meniscus for all nanopores and our results show that smaller nanopores would have more extended menisci and thus more evaporation area inside the nanopores. Such difference of the meniscus shape thus would lead to the observed large difference between the theoretical predictions and the reported experimental results and smaller nanopores are expected to show larger difference. This figure is significant because it demonstrates the importance of carefully designing the conduit hydraulic resistance at a known working temperature - we can simply engineer the conduit geometry profile and increase the hydraulic resistance to obtain a fully extended meniscus, leading to a higher evaporation mass flux. This is in contradictory to the mainstream articles [3,10,11,25,38] where the hydraulic resistance is minimized with multi-tier structures.

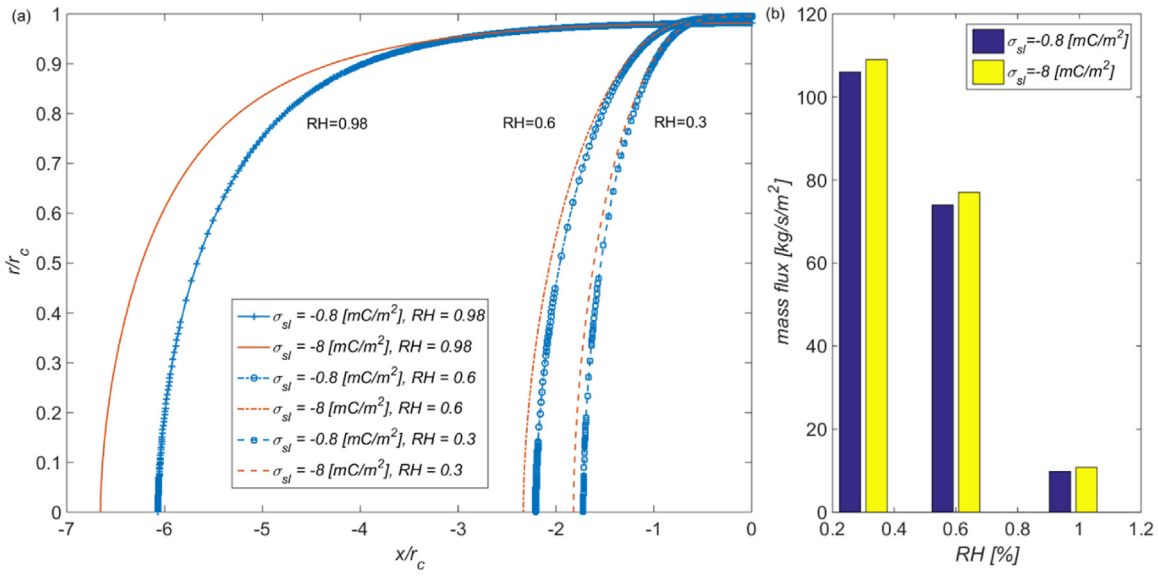

Fig. 13. Effect of relative humidity on the meniscus shape and the evaporation mass flux. (a) The relative humidity effect on the meniscus shape with different surface charge densities corresponding to $r = 50$ **nm** T = 90 [°**C**]. Lines with markers represent a surface charge density of -0.8 [**mC**/**m²**] while lines without markers represent a surface charge density of -8 [**mC**/**m²**]. (b) The corresponding evaporation mass flux [**kg**/**m²s**] at two different surface charge densities.

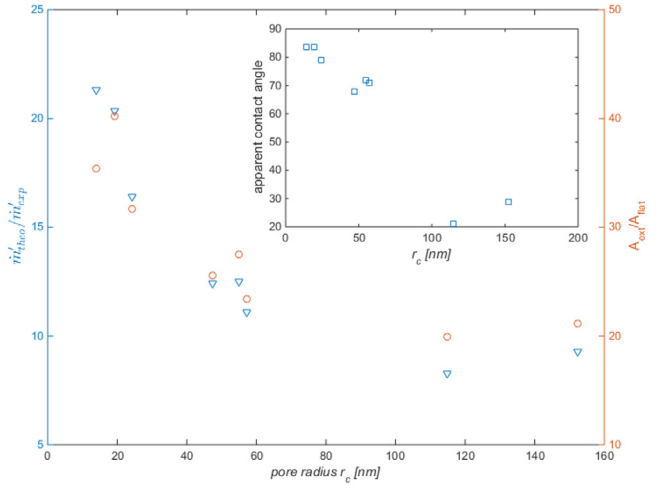

Fig. 14. The ratio of theoretically computed mass flux versus experiment data obtained from [12] with $T_w = 20$ [°**C**], $P_v = 150$ [**Pa**] and $RH = 0.3$. The inset figure shows the apparent contact angle as a function of pore radius obtained from [12].

Finally, it is worth pointing out the difference of the fundamental mechanism leading to the increase of evaporation mass flux in this work and in [12]. In Li's hypothesis, the proton concentration inside the nanopore regime is the key factor, and the evaporation flux would be higher given a higher proton concentration. Hence, as the pore diameter becomes smaller, the proton concentration would increase due to the charge conservation equation as the electrical double layer overlaps with each other, $[\mathbf{H_3O^+}] \propto r^{-1}$. This would lead to a higher evaporation mass flux even if the meniscus is flat, as reported in their SI. However, in this analysis, the mechanism that leads to an increase in the mass flux is due to a larger evaporating area inside the pore. Thus, if the meniscus shape remains flat, the evaporation flux would not increase as the pore radius decreases. Furthermore, the accommodation factor increases as the pore radius decreases in [12] while in this work, the evaporation coefficient remains a constant $\hat{\sigma} = 0.3$, which is in line with [25]. Further experiments and simulations should be conducted to address these issues and to verify the effect of surface charges on evaporation kinetics.

It is worth noting that we only model traditional hydrophilic nanopores in this study where the nanopore surface in contact with the water is hydrophilic and the thickness of the nanopore is hundreds of nanometers. We believe only contact angle below 90 ° can induce negative liquid pressure and capillary flow to ensure liquid water supply to the evaporation interface. Since hydrophobic pores do not provide such characteristics in theory, our model would not apply to this situation. It is also note worthy that a recent article published by Xiao et al. [39] did evaporation experiments with graphene nanopores and claimed that such nanopore device had a better performance than SiN counterparts under a pore diameter of 60 [**nm**]. However, since the contact angle of graphene is still on a heated debate [40,41] and the membrane is only an atom thick, we avoid comparing their experiment data with this study to prevent further confusion. Further development is needed for addressing the theoretical maximum evaporation mass flux for hydrophobic pores and the thickness effect of the membrane on the evaporation kinetics.

4. Conclusions

A theoretical analysis is carried out to study the surface charge effect on the evaporation area of the kinetically-limited evaporation. This is achieved by considering the molecular interaction between the solid, liquid and the ions dissolved in the solution. The coupled systems of equations for the fluid flow, heat transfer, and stress balance along the liquid-vapor interface are solved numerically to unravel the meniscus shape, the pressure distribution inside the pore regime, and the corresponding average mass flux during evaporation. Major remarks are summarized as follow:

- The effect of increasing the magnitude of the solid-liquid surface charge density is found to always extend the meniscus at a given working condition, leading to a remarkable 121% increment when charging the wall to -100 [**mC**/**m²**]. Meanwhile, the classical Schrage equation underestimates the mass flux by 77.5%. This is attributed to the attractive electrostatic force between the charged solid wall and the counter-ions that increases the disjoining pressure and reducing the gradient of

the curvature near the wall. This result is significant since we could simply charge the evaporation surface to increase the performance of a thermal management device without consuming remarkable energy.

- The effect of increasing the liquid-vapor surface charge density is found to also extend the meniscus at a given working condition. The mass flux increased from 107 to 170 $\mathbf{kg/m^2s}$.
- The effect of decreasing the pore radius on charged walls is to further extend the regime where the disjoining pressure is significant. This leads to the extension of meniscus for smaller capillaries and a higher average mass flux.
- The effect of increasing the temperature and decreasing the relative humidity on charged walls are found to be comparable. They both lead to an increased potential for evaporation as the kinetically-limited evaporation is only a function of the pressure difference at the interface.
- By comparing the theoretical work with available literature data, we point out that tailoring proper hydraulic resistance for a conduit at a given working condition in a thermal management device is important to optimize the average mass flux and this is achieved by extending the meniscus. On the other hand, the fundamental mechanism for enhancing the average mass flux is shown to be diverging from the existing literature. Further experiment and simulation effort is called to address these discrepancies.

Declaration of Competing Interest

The authors declare the following financial interests/personal relationships which may be considered as potential competing interests:

Chuanhua Duan reports financial support was provided by National Science Foundation.

CRediT authorship contribution statement

Chu-Yao Chou: Conceptualization, Methodology, Software, Formal analysis, Visualization, Investigation, Writing – original draft. **Chuanhua Duan:** Conceptualization, Methodology, Writing – review & editing, Funding acquisition, Supervision.

Data availability

Data will be made available on request.

Acknowledgments

This work was supported by the National Science Foundation (CBET-1653767 and CBET-1805421).

References

[1] S. Adera, D. Antao, R. Raj, E.N. Wang, Design of micropillar wicks for thin-film evaporation, Int. J. Heat Mass Transf. 101 (2016) 280–294.
[2] M. Bulut, S.G. Kandlikar, N. Sozbir, A review of vapor chambers, Heat Transf. Eng. 40 (19) (2019) 1551–1573.
[3] S. Narayanan, A.G. Fedorov, Y.K. Joshi, Heat and mass transfer during evaporation of thin liquid films confined by nanoporous membranes subjected to air jet impingement, Int. J. Heat Mass Transf. 58 (1–2) (2013) 300–311.
[4] H. Ghasemi, G. Ni, A.M. Marconnet, J. Loomis, S. Yerci, N. Miljkovic, G. Chen, Solar steam generation by heat localization, Nat. Commun. 5 (2014) 4449.
[5] P. Tao, G. Ni, C. Song, W. Shang, J. Wu, J. Zhu, G. Chen, T. Deng, Solar-driven interfacial evaporation, Nat. Energy 3 (12) (2018) 1031–1041.
[6] G. Xue, Y. Xu, T. Ding, J. Li, J. Yin, W. Fei, Y. Cao, J. Yu, L. Yuan, L. Gong, et al., Water-evaporation-induced electricity with nanostructured carbon materials, Nat. Nanotechnol. 12 (4) (2017) 317–321.
[7] C. Chen, Y. Kuang, L. Hu, Challenges and opportunities for solar evaporation, Joule 3 (3) (2019) 683–718.
[8] N.H. Aly, A.K. El-Figi, Mechanical vapor compression desalination systems-a case study, Desalination 158 (1–3) (2003) 143–150.
[9] A. Yaroshchuk, Evaporation-driven electrokinetic energy conversion: critical review, parametric analysis and perspectives, Adv. Colloid Interface Sci. (2022) 102708.
[10] Z. Lu, K.L. Wilke, D.J. Preston, I. Kinefuchi, E. Chang-Davidson, E.N. Wang, An ultrathin nanoporous membrane evaporator, Nano Lett. 17 (10) (2017) 6217–6220.
[11] D.F. Hanks, Z. Lu, J. Sircar, T.R. Salamon, D.S. Antao, K.R. Bagnall, B. Barabadi, E.N. Wang, Nanoporous membrane device for ultra high heat flux thermal management, Microsyst. Nanoeng. 4 (1) (2018) 1–10.
[12] Y. Li, H. Chen, S. Xiao, M.A. Alibakhshi, C.-W. Lo, M.-C. Lu, C. Duan, Ultrafast diameter-dependent water evaporation from nanopores, ACS Nano 13 (3) (2019) 3363–3372.
[13] P.G.d. Gennes, et al., Wetting: statics and dynamics, Rev. Mod. Phys 57 (3) (1985) 827–863.
[14] P.C. Wayner Jr., Y.K. Kao, L.V. LaCroix, The interline heat-transfer coefficient of an evaporating wetting film, Int. J. Heat Mass Transf. 19 (5) (1976) 487–492.
[15] P.C. Wayner Jr., Effect of thin film heat transfer on meniscus profile and capillary pressure, AIAA J. 17 (7) (1979) 772–776.
[16] C. Buffone, K. Sefiane, Investigation of thermocapillary convective patterns and their role in the enhancement of evaporation from pores, Int. J. Multiphase Flow 30 (9) (2004) 1071–1091.
[17] C. Buffone, K. Sefiane, J. Christy, Experimental investigation of the hydrodynamics and stability of an evaporating wetting film placed in a temperature gradient, Appl. Therm. Eng. 24 (8–9) (2004) 1157–1170.
[18] H. Wang, J.Y. Murthy, S.V. Garimella, Transport from a volatile meniscus inside an open microtube, Int. J. Heat Mass Transf. 51 (11–12) (2008) 3007–3017.
[19] S.-K. Wee, K.D. Kihm, K.P. Hallinan, Effects of the liquid polarity and the wall slip on the heat and mass transport characteristics of the micro-scale evaporating transition film, Int. J. Heat Mass Transf. 48 (2) (2005) 265–278.
[20] S. DasGupta, J.A. Schonberg, P.C. Wayner Jr., Investigation of an evaporating extended meniscus based on the augmented young–laplace equation, J Heat Transf. 115 (1) (1993) 201–208.
[21] L.W. Swanson, G.C. Herdt, Model of the evaporating meniscus in a capillary tube, J. Heat Transf. 114 (2) (1992) 434–441.
[22] S. Narayanan, A.G. Fedorov, Y.K. Joshi, Interfacial transport of evaporating water confined in nanopores, Langmuir 27 (17) (2011) 10666–10676.
[23] S. Pati, S.K. Som, S. Chakraborty, Combined influences of electrostatic component of disjoining pressure and interfacial slip on thin film evaporation in nanopores, Int. J. Heat Mass Transf. 64 (2013) 304–312.
[24] Z. Lu, S. Narayanan, E.N. Wang, Modeling of evaporation from nanopores with nonequilibrium and nonlocal effects, Langmuir 31 (36) (2015) 9817–9824.
[25] Z. Lu, I. Kinefuchi, K.L. Wilke, G. Vaartstra, E.N. Wang, A unified relationship for evaporation kinetics at low mach numbers, Nat. Commun. 10 (1) (2019) 1–8.
[26] R.W. Schrage, A Theoretical study of Interphase Mass Transfer, Columbia University Press, 1953.
[27] J.R. Philip, Unitary approach to capillary condensation and adsorption, J. Chem. Phys. 66 (11) (1977) 5069–5075.
[28] B.V. Derjaguin, N.V. Churaev, Structural component of disjoining pressure, J. Colloid Interface Sci. 49 (2) (1974) 249–255.
[29] I. Langmuir, Repulsive forces between charged surfaces in water, and the cause of the Jones-Ray effect, Science 88 (2288) (1938) 430–432.
[30] V.P. Carey, Liquid-Vapor Phase-Change Phenomena: An Introduction to the Thermophysics of Vaporization and Condensation Processes in Heat Transfer Equipment, CRC Press, 2020.
[31] J.N. Israelachvili, Intermolecular and Surface Forces, Academic press, 2011.
[32] E. Poli, K.H. Jong, A. Hassanali, Charge transfer as a ubiquitous mechanism in determining the negative charge at hydrophobic interfaces, Nat. Commun. 11 (1) (2020) 1–13.
[33] S.H. Behrens, D.G. Grier, The charge of glass and silica surfaces, J. Chem. Phys. 115 (14) (2001) 6716–6721.
[34] A. Zou, S. Poudel, M. Gupta, S.C. Maroo, Disjoining pressure of water in nanochannels, Nano Lett. 21 (18) (2021) 7769–7774.
[35] K.R. Bagnall, Device-level thermal analysis of GaN-based electronics, Massachusetts Institute of Technology, 2013 Ph.D. thesis.
[36] M. Himanshu, Proton transfers at the air-water interface, California Institute of Technology, 2013 Ph.D. thesis.
[37] S. Zhou, Z. Xiong, F. Liu, H. Lin, J. Wang, T. Li, Q. Han, Q. Fang, Novel Janus membrane with unprecedented osmosis transport performance, J. Mater. Chem. A 7 (2) (2019) 632–638.
[38] Z. Lu, T.R. Salamon, S. Narayanan, K.R. Bagnall, D.F. Hanks, D.S. Antao, B. Barabadi, J. Sircar, M.E. Simon, E.N. Wang, Design and modeling of membrane-based evaporative cooling devices for thermal management of high heat fluxes, IEEE Trans. Compon. Packag. Manuf. Technol. 6 (7) (2016) 1056–1065.
[39] S. Xiao, K. Meng, Q. Xie, L. Zhai, Z. Xu, H. Wang, C. Duan, Edge-enhanced ultrafast water evaporation from graphene nanopores, Cell Rep. Phys. Sci. (2022) 100900.
[40] A.V. Prydatko, L.A. Belyaeva, L. Jiang, L. Lima, G.F. Schneider, Contact angle measurement of free-standing square-millimeter single-layer graphene, Nat. Commun. 9 (1) (2018) 1–7.
[41] L.A. Belyaeva, G.F. Schneider, Wettability of graphene, Surf. Sci. Rep. 75 (2) (2020) 100482.